A Classification of Clay-Rich Subaqueous Density Flow Structures

Hermidas, Navid; Eggenhuisen, Joris T.; Jacinto, Ricardo Silva; Luthi, Stefan M.; Toth, Ferenc; Pohl, Florian

DOI
10.1002/2017JF004386

Publication date
2018

Document Version
Final published version

Published in
Journal of Geophysical Research: Earth Surface

Journal of Geophysical Research: Earth Surface

RESEARCH ARTICLE
10.1002/2017JF004386

Key Points:
- Four distinct flow structures for muddy density flows were observed
- Dependence of the deposit emplaced by a subaqueous density flow on its flow structure was examined
- Upscaling of small flume experiments to large-scale natural density flows was investigated

Correspondence to:
N. Hermidas,
N.Hermidas@tudelft.nl

Citation:
Hermidas, N., Eggenhuisen, J. T., Jacinto, R. S., Luthi, S. M., Toth, F., & Pohl, F. (2018). A classification of clay-rich subaqueous density flow structures. *Journal of Geophysical Research: Earth Surface*, *123*. https://doi.org/10.1002/2017JF004386

Received 6 JUN 2017
Accepted 26 MAR 2018
Accepted article online 6 APR 2018

A Classification of Clay-Rich Subaqueous Density Flow Structures

Navid Hermidas[1], Joris T. Eggenhuisen[2], Ricardo Silva Jacinto[3], Stefan M. Luthi[1], Ferenc Toth[4], and Florian Pohl[2]

[1]Faculty of Civil Engineering and Geosciences, Delft University of Technology, Delft, Netherlands, [2]Department of Earth Sciences, Utrecht University, Utrecht, Netherlands, [3]Marine Geosciences Unit, Ifremer, France, [4]Faculty of Science and Informatics, University of Szeged, Szeged, Hungary

Abstract This study presents a classification for subaqueous clay-laden sediment gravity flows. A series of laboratory flume experiments were performed using 9%, 15%, and 21% sediment mixture concentrations composed of sand, silt, clay, and tap water, on varying bed slopes of 6°, 8°, and 9.5°, and with discharge rates of 10 and 15 m^3/hr. In addition to the characteristics of the boundary and plug layers, which have been previously used for the classification of open-channel clay-laden flows, the newly presented classification also incorporates the treatment of the free shear layer. The flow states within the boundary and free shear layers were established using calculation of the inner variable, self-similarity considerations, and the magnitude of the apparent viscosity. Based on the experimental observations four flow types were recognized: (1) a clay-rich plug flow with a laminar free shear layer, a plug layer, and a laminar boundary layer, (2) a top transitional plug flow containing a turbulent free shear layer, a plug layer, and a laminar boundary layer, (3) a transitional turbidity current with a turbulent free shear layer, no plug layer, and a laminar boundary layer, and (4) a fully turbulent turbidity current. A connection between the emplaced deposits and the relevant flow types is drawn and it is shown that a Froude number, two Reynolds numbers, and a dimensionless yield stress parameter are sufficient to associate an experimental flow type with a natural large-scale density flow.

Plain Language Summary Deposits of submarine density flows can be important hydrocarbon reservoirs. Quality of these reservoirs is primarily controlled by grain size and clay concentration of the sediment mixture at the time of deposition. These parameters are dictated by the structures of the sediment carrying flow at the time of deposition. This study proposes a classification for muddy subaqueous density flows based on the flow structures. According to this classification a clay-rich flow may fall within one of four distinct flow types: (1) a cohesive plug flow with laminar free shear and boundary layers and a plug, (2) a top transitional plug flow containing a turbulent free shear layer, a plug layer, and a laminar boundary layer, (3) a transitional turbidity current with a turbulent free shear layer and a laminar boundary layer, and (4) a turbulent turbidity current. A connection between the emplaced deposit and the relevant flow type is drawn through the results obtained from flume experiments. It is proposed that a Froude number, a boundary layer Reynolds numbers, a free shear layer Reynolds number, and a dimensionless yield stress parameter are sufficient to connect a flow type with a natural large-scale density flow.

1. Introduction

Volumetrically, submarine sediment density flows are the most dominant sediment transport mechanism on our planet (Talling et al., 2012). Such flows have resulted in the formation of some of the thickest depositional accumulations on Earth. Enhanced understanding of their occurrence, evolution, and deposition are beneficial for predicting recurrence interval of large tsunamis and protection of offshore infrastructure against natural hazards (Arai et al., 2013; Mulder & Cochonat, 1996). Furthermore, in 1999 it was estimated that the deposits of these flows host approximately 1200 to 1300 oil and gas fields (Stow & Mayall, 2000), many of which are giants (>500 million barrels oil equivalent). The discovery of such oil and gas fields has considerably increased in the past decades, particularly in offshore settings. The quality of oil and gas reservoirs is primarily controlled by grain size and clay concentration of the flows that deposit these sediments

(Kane & Pontén, 2012; Kane et al., 2016). Therefore, for prediction purposes it has become of paramount importance to connect the dynamics of clay-carrying density flows to their depositional characteristics.

If initiated by a triggering event such as a sediment slide, a subaqueous density flow goes through a wide range of transformations in both space and time (Talling et al., 2007). In its initial state, such a flow is often composed of blocky material which disintegrates due to shearing and pressure (Schwarz, 1982). The resulting flow, which can be classified as debris flow, is laminar, dense, and cohesive (Talling et al., 2012).

As the flow moves toward equilibrium, depending on its boundary conditions, it may speed up or slow down, deposit sediment, erode the substrate, contract in the form of the tail approaching the head, stretch, entrain water and grow in height, or dewater and collapse. If the combined rates of sediment incorporation due to erosion, contraction, and dewatering of the flow is higher than those of sediment deposition, stretching, and water entrainment, the flow becomes denser, and if it is clay-bearing, more cohesive. The velocity profile of such a flow transforms toward that of a plug flow (PF), which is dense and laminar within the boundary and free shear layers and whose primary sediment support mechanism is not turbulence. On the contrary, if the combined rates of deposition, stretching, and water entrainment is higher than those of sediment incorporation due to erosion, contraction, and dewatering, the flow becomes more dilute and less cohesive, and the velocity profile of such a flow transforms toward that of a turbidity current. Flows between these two end members are known as transitional flows (Haughton et al., 2009; Kane & Pontén, 2012; Talling et al., 2012).

Several attempts have been made in the past to connect structures of transitional density flows to their resulting deposits. Felix et al. (2009) presented a generic classification scheme for flows transitional between a concentrated debris flow and a high-density turbidity current. In their work they connect five distinct flow types with their possible resulting deposit based on concentration and rheological properties of the fluid. The structures of the flows producing these deposits, however, are not fully explored or quantified in their work. In this work we focus on the flow structures and aim to connect the resulting deposits to the flow structures. Baas et al. (2009) studied turbulent properties of transitional flows and presented a phase diagram for clay-laden open-channel flows on the basis of the balance between turbulent and cohesive forces. Following this work, they then studied the behavior of rapidly decelerating flows of mixtures of sand, silt, and clay and the influence of variations in clay concentration on the bed forms and the stratification produced (Baas et al., 2011). Sumner et al. (2009) used flume experiments to investigate linked debrite-turbidite deposits of waning density flows composed of a fixed amount of sand and variable mud fractions. In their work, they recognized four different deposit types which they then connected to the phase diagram of Baas et al. (2009). The contributions following from the work of Baas et al. (2009) illuminate depositional types as related to flow structure for clay-rich open-channel flows. Such a classification does not exist for clay-rich subaqueous density flows. While the flow structure of turbidity currents is relatively well understood (Altinakar et al., 1996; Islam & Imran, 2010; Kneller et al., 1999; Meiburg & Kneller, 2010), the flow structure of subaqueous clay-rich density currents that are thought to deposit hybrid beds has not been comprehensively documented yet (Felix et al., 2009). Manica (2012) performed a series of lock-exchange experiments on sediment gravity flows based on which six flow types were recognized according to the hydrodynamic, depositional, and rheological properties of the flows. He then connected the spatial evolution of these flows and their deposits to the flow types. The work of Manica (2012) presents an in-depth analysis of the effects of sediment concentration and rheological effects of clay on the deposition processes. However, it does not provide a quantified view of the vertical flow structures based on nondimensional parameters. Here we aim to expand on this front.

The aims of this paper are threefold: (1) To present a classification of flow types intermediate between end-member debris flows and turbidity currents based on observed flow structures; (2) To link the flow types to their typical deposits; and (3) To present a set of scaling parameters that can be used to relate small-scale flume experiments to the large-scale natural flows.

To this end, a series of experimental runs were performed on mixtures composed of (1) sand, silt, clay, and water and, (2) sand, clay, and water. During the experiments the sediment concentration of the mixture, the bed slope, and the discharge rate were systematically varied. Velocity data were obtained using two Ultrasonic Doppler Velocity probes and rheometry measurements were performed on the mixtures to obtain apparent viscosity data. Three regions were then recognized within the velocity profile of a density flow. Reynolds number, Froude number, and yield stress were calculated in order to classify and scale subaqueous density flows. The resulting deposit from each experimental run was analyzed to make the connection to the types of flows.

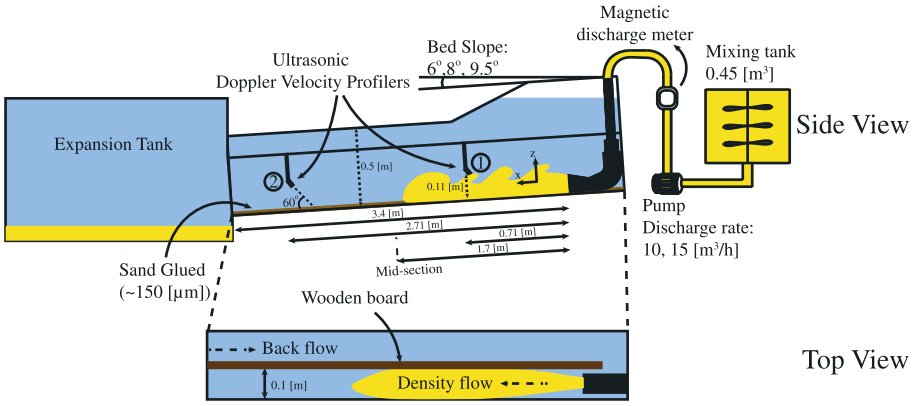

Figure 1. Sketch of the flume at the Eurotank Laboratory of Utrecht University.

2. Methods

In section 2.1 the experimental setup is explained. In section 2.2, three length scales are introduced which are used in section 2.7 to define a set of dimensionless parameters. In order to evaluate the regime of the flow within the boundary and free shear layers, sections 2.3–2.6 present the procedures that are followed for the various necessary parametrizations of the results. Finally, for scaling purposes, a Froude number, two Reynolds numbers for the boundary and free shear layers, and a dimensionless yield stress parameter are defined in section 2.7.

2.1. Experimental Setup

Experiments were performed in a 3.7 m long, 0.22 m wide, and 0.5 m high flume with glass side walls and an adjustable slope located at the Eurotank Laboratory at Utrecht University (Figure 1). To mitigate back flow, a wooden board was used to split the flume into two sections of 0.10 m wide (top view in Figure 1). Quartz sand from Sibelco with a median diameter of 150 μm was glued on the nonerodible bed to provide roughness.

Glass granules obtained from Kuhmichel Abrasiv B.V. in the Netherlands with a median diameter of 46 μm was used as silt material and Crown Kaolinite clay from ActiveMinerals International, with a median diameter of 0.18 μm was used as clay material (Figure 2). The same quartz sand material as the one glued to the bed was used to prepare the mixtures.

In order to incorporate the influences of sediment composition in this study, 14 runs were performed with sand, clay, and tap water and 15 runs were performed with sand, silt, clay, and tap water. The sediment volume concentration was varied between 9%, 15%, and 21% and contained 2/3 sand and 1/3 clay for the

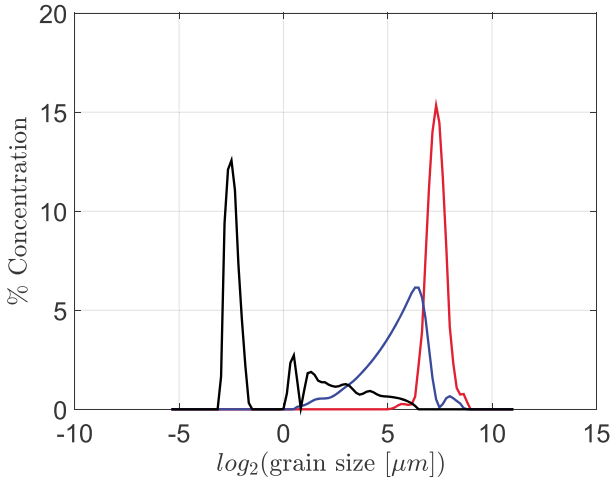

Figure 2. Grain size distribution of silt (blue), sand (red), and clay (black), obtained from Malvern grain size analysis.

Table 1
Slope, Discharge Rate, and Sediment Concentration of Each Run

Run no.	Slope	Discharge rate $\frac{m^3}{hr}$	Sed. vol.%	Silt in mix. vol.%	Fr_1	Fr_2	$Re_{\mu,BL1}$	$Re_{\mu,BL2}$	$Re_{\mu,FSL1}$	$Re_{\mu,FSL2}$
1	6°	10	15	5	1	1.3	217	57	781	109
2	6°	10	15	0	0.7	0.6	52	34	106	27
3	9.5°	10	15	0	0.9	1.2	24	31	77	92
4	8°	10	15	0	1	1.2	95	123	316	216
7	8°	15	15	0	1.3	1.4	367	140	1,806	770
8	9.5°	15	9	0	1	1.1	1,944	2,288	20,112	15,810
9	6°	10	9	0	0.7	1	2,150	1,325	14,758	4,811
10	9.5°	15	15	0	1.2	1.5	305	81	1,788	539
11	6°	15	15	0	1.4	1.2	504	86	1792	271
12	6°	15	9	0	0.9	1	1,307	2,259	10,350	13,100
13	8°	15	21	0	1	0.9	31	21	156	36
15	9.5°	10	21	0	0.9	1	22	23	40	27
16	8°	10	21	7	1	1.3	23	22	51	40
17	9.5°	10	21	7	1.5	2	38	32	103	59
18	6°	10	21	7	1	1.1	42	21	116	23
19	8°	10	15	5	1.1	1.4	160	145	685	493
20	9.5°	10	15	5	1.2	1.4	131	218	633	1,224
21	6°	15	15	5	1.1	1.2	295	83	2,260	298
22	8°	15	15	5	1.2	1.3	322	74	2,225	480
23	9.5°	15	15	5	1.2	1.5	140	65	888	392
24	6°	15	21	7	1.3	1.2	53	48	300	84
25	6°	10	9	3	0.8	1	2,179	2,205	10,216	7,806
26	6°	15	9	3	1	0.9	2,287	2,938	16,449	14,220
27	9.5°	15	21	7	1.4	1.8	88	48	566	190
28	8°	15	21	7	1.3	1.4	47	21	193	70
29	8°	10	21	0	0.6	0.5	12	8	22	8
30	9.5°	15	21	0	1.1	1.1	55	46	240	94
31	9.5°	10	9	3	1	1.2	1,937	3,178	14,319	21,328
32	9.5°	10	9	0	0.8	1.3	1,891	1,919	14,472	12,710

Note. Subscripts 1 and 2 signify information at the location of UVP1 and UVP2. UVP = Ultrasonic Doppler Velocity Profiler.

runs without silt and 1/3 sand, 1/3 silt, and 1/3 clay, for the runs including silt. An overview of the runs is given in Table 1.

The data from some of the runs were omitted from the data set. Runs 5 and 6 failed due to technical issues and were omitted from the data set. For run 14, a mixture with a 30% sediment concentration was pumped onto a 9.5° bed slope. Upon entering the flume the sediment deposited immediately and, therefore, no flow velocity could be measured. The data for this run were therefore omitted from the data set. Some mixtures had different pH levels compared to others. Runs containing silt were basic and had a pH close to 10. This resulted in less flocculation for these runs compared to those without silt, which had a pH of approximately 5.

Before the experiments the mixture was stirred for 30 min to 2 hr in a 0.45 m^3 mixing tank and the flume was filled with tap water. The sediment mixture was then pumped into the flume. The discharge rate was monitored by a magnetic discharge meter (Krohne Optiflux 2300) and regulated to 10 or 15 m^3/hr by a Labview control system. Upon exiting the flume the sediment mixture flowed into an expansion tank (Figure 1) such that reflections had a minimal impact on the experimental measurements.

To obtain velocity profile measurements, two Ultrasonic Doppler Velocity Profiler (UVP) probes (Duo MX, 1 MHz) were placed at 0.7 and 2.7 m distance from the inlet, at a height of 0.11 m above the bed and with an angle of 60° to the bed, facing upstream (Figure 1). Each probe emitted and received 32 bursts,

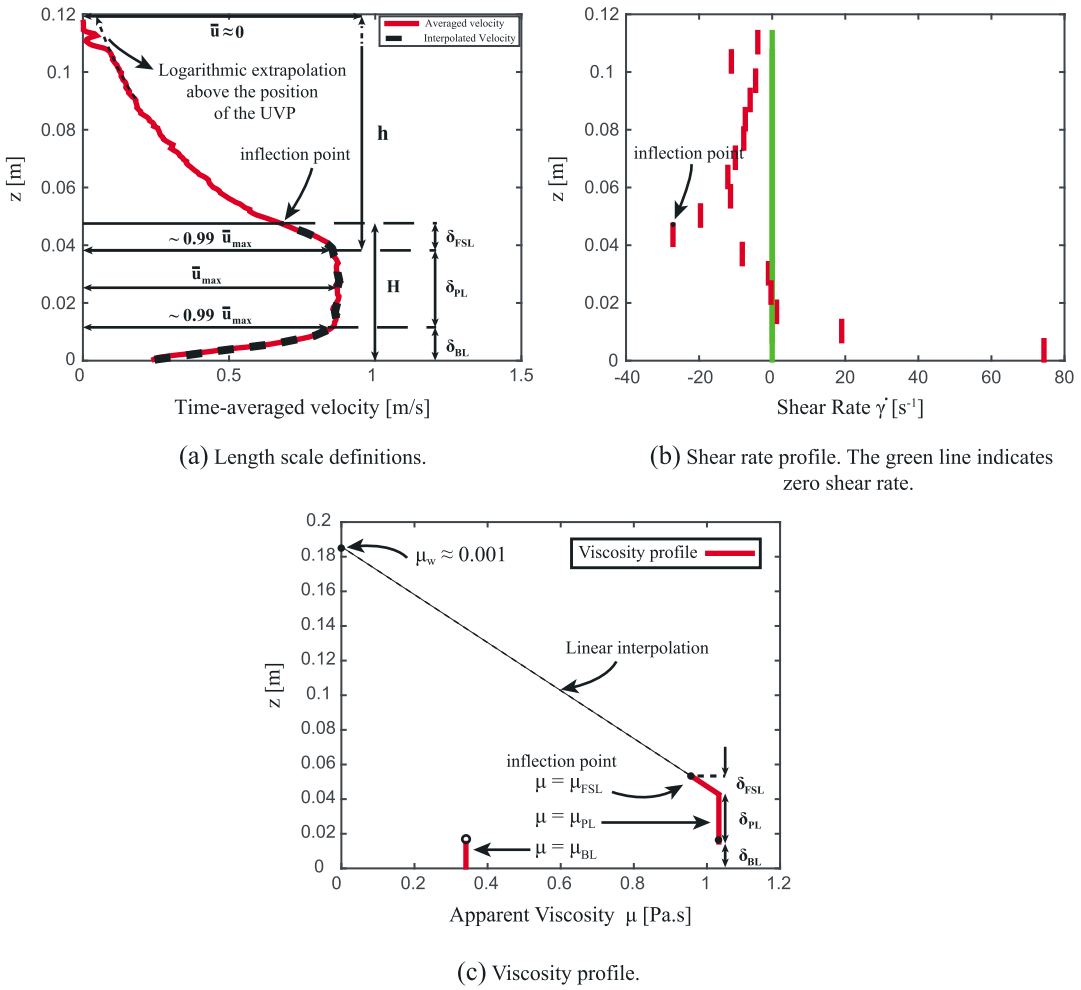

(a) Length scale definitions.

(b) Shear rate profile. The green line indicates zero shear rate.

(c) Viscosity profile.

Figure 3. A representative example of experimental measurements: (a) Free shear layer, plug layer, and boundary layer length scales, (b) shear rate profile, and (c) viscosity profile, for run 15. The dotted black line in (a) depicts the interpolated velocity data. The boundary layer viscosity, μ_{BL}, and the plug layer viscosity, μ_{PL}, in (c) were obtained by averaging the viscosity data within the boundary and plug layers. Within the free shear layer the viscosity was obtained by linear interpolation, as will be explained in section 2.3.

followed by a dead time of approximately 10 ms before the burst sequence of the second probe. The duration of each burst was 5 μs. The time resolution of a burst sequence was 0.16 ms. The time between successive burst sequences of a single probe was 0.22 s. The thickness of a measurement bin along the *z* direction was 0.64 mm. The velocities parallel to the bed were calculated from the measurements and used to obtain a velocity profile. The total duration of each flume measurement was approximately 1 min and was long enough to obtain a steady state velocity profile.

2.2. Length Scale Definitions

Clay-rich sediment density flows consist of three vertically stacked regions: (1) a free shear layer at the top, (2) a plug layer, and (3) a basal boundary layer. Therefore, three length scales, δ_{FSL}, δ_{PL}, and δ_{BL} can be attributed to the sizes of the free shear layer, the thickness of the plug layer, and the thickness of the boundary layer, respectively. These are depicted in Figure 3a. The boundary layer thickness, δ_{BL}, is defined as the distance from the bed to the position where the time-averaged velocity, $\bar{u}$, becomes approximately equal to 0.99 $\bar{u}_{max}$, where $\bar{u}_{max}$ is the maximum time-averaged velocity above the bed. The plug layer thickness, δ_{PL}, is defined as the distance above the boundary layer to the position where the time-averaged velocity first falls below approximately 0.99 $\bar{u}_{max}$ (Figure 3a). The free shear layer thickness is defined as the distance from the top of the plug layer to the point of maximum vorticity, called the inflection point. The flow height, *H*, is defined as the distance from the bed to the inflection point (Figure 3a).

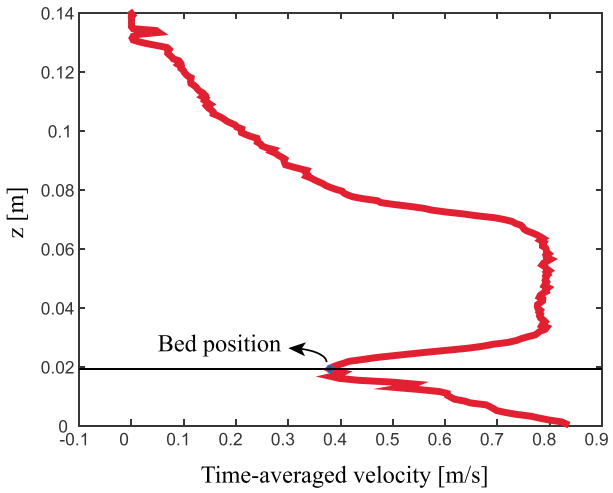

Figure 4. Bed position obtained from the Ultrasonic Doppler Velocity Profiler data of run 15.

In order to obtain the position of the bed, that is, the position of the top of the deposit emplaced over the bottom of the tank, the time-averaged velocity ($\bar{u}$) profile data obtained from the transceiver were used to pinpoint the position of the minimum velocity coinciding with approximately the distance of the UVP from the bed, as demonstrated for a typical velocity profile result in Figure 4. The profile recorded below the bed position in Figure 4 is due to the data received after the signal is reflected off the bed. Close to the bed, the measurement volume spans from the bed to a certain location above the bed. Consequently, within this measurement volume the velocity of the fluid varies from zero, at the bed, to a nonzero value, above the bed. Since postprocessing is performed on the velocity recordings made from this finite measurement volume in the vicinity of the bed, the resulting velocity at the bed is not assigned a zero value.

The position of the inflection point was obtained by first linearly interpolating the velocity data over approximately 17 uniformly spaced elements (for some runs different number of elements resulted in a better accuracy) and then differentiating the resulting curve to obtain a shear rate profile (Figure 3b). The element with the minimum shear rate was then associated with the inflection point. For computational purposes, the position of the top of the element corresponding to the inflection point was used as the vertical position of the inflection point (Figure 3b). The accuracy of pinpointing the vertical position of the inflection point from this process was approximately 0.006 m, that is, each element spanned a vertical distance of approximately 0.006 m.

For some of the runs the velocity data extended above the position of the UVP; therefore, logarithmic extrapolation was used to estimate the position where the time-averaged velocity first became zero in the top part of the flow (Figure 3a). The distance from the top of the plug layer to the position where the time-averaged velocity is approximated to be zero is called h (Figure 3a).

2.3. Laminar Apparent Viscosity Measurements

The apparent viscosity of the flow can carry important information regarding the regime of the flow. In this section we present the procedure that was followed for obtaining laminar apparent viscosity data for the sediment mixtures. This laminar apparent viscosity data will be used (1) to evaluate the regime of the flow and (2) to define dimensionless parameters in section 2.7.

The occurrence of clay in a density flow can greatly influence its behavior (Pratson et al., 2000). The fluid in clay-laden flows is thixotropic, viscoelastic, and shear thinning (Coussot, 1997). For such fluids, in steady state, the relation between shear stress, τ, and shear rate can be expressed as

$$\tau = \mu(C, \dot{\gamma})\dot{\gamma}, \tag{1}$$

where μ is the apparent viscosity, C is the concentration, and $\dot{\gamma}$ is the shear rate.

The apparent viscosities of the mixtures used in the experiments were measured in a rheometer. Mixtures containing the same sediment composition and concentration as presented in Table 1 were prepared. Stress controlled tests were performed on these mixtures using an MRC302 Anton Paar rheometer, and the apparent

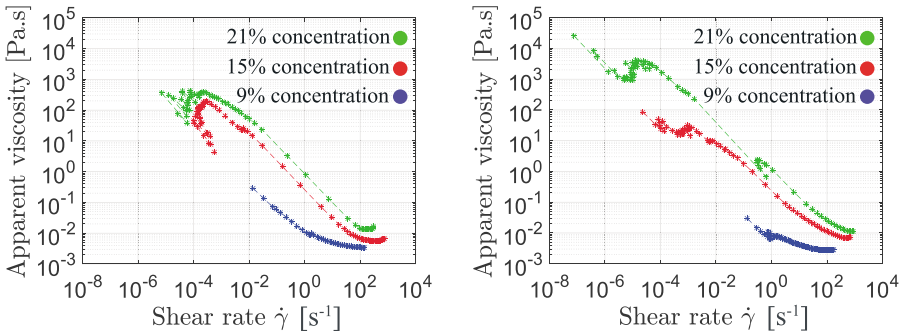

(a) Apparent viscosity versus shear rate data for sand-clay-water mixtures.

(b) Apparent viscosity versus shear rate data for sand-silt-clay-water mixtures.

Figure 5. Apparent viscosity versus shear rate data obtained from stress controlled tests for (a) sand-clay-water mixtures and (b) sand-silt-clay-water mixtures. Mixtures with 21% sediment concentration are shown in green, those with 15% sediment concentration are shown in red, and those with 9% sediment concentration are shown in blue.

viscosity was measured at various shear rates (Figure 5). In order to prolong the settling duration the concentric cylinder geometry was used. The duration of the measurement for obtaining each data point was chosen to be 10 s and was considered long enough to ensure near-equilibrium conditions. For shear rates lower than approximately 10^{-3} s^{-1}, the precision of the measurements was low for mixtures of 15% and 21% sediment concentration (Figure 5). Therefore, for computational purposes only apparent viscosity data obtained for shear rates between 10^{-3} s^{-1} and approximately 100 s^{-1} were considered. Figure 5 shows that in general, sand-silt-clay-water mixtures had lower apparent viscosities compared to the sand-clay-water mixtures.

Since the head of the flow was not the subject of the current study, the effects of hydroplaning were neglected and the density of the fluid within the boundary and plug layers was assumed to be equal to that of the fluid within the mixing tank (Mohrig et al., 1998). Therefore, it was assumed that the apparent viscosity measured with the rheometer corresponds to the apparent viscosity of the fluid within the boundary and plug layers and varies only as a function of the shear rate at these locations (equation (1)). The apparent viscosities corresponding to the shear rates obtained from the velocity data, as in Figure 3b, were then obtained from the rheometer measurements by interpolating the apparent viscosity data for different shear rates and reading off the corresponding values. The number of elements used for interpolating the shear rate data were therefore accordingly adjusted for some runs to avoid an element having a shear rate lower than 10^{-3} s^{-1} within, for example, the plug layer region (Figure 3b). Consequently, for every shear rate profile obtained from velocity data, an apparent viscosity profile was obtained for the boundary and the plug layers. The apparent viscosity profile was then averaged within these two regions to obtain a mean viscosity for the boundary layer, here referred to as μ_{BL}, and a mean viscosity for the plug layer, here referred to as μ_{PL}.

Within the free shear layer and above the inflection point (specified as h in Figure 3a) the apparent viscosity varies between μ_{PL} at the plug and that of water, $\mu_w = 0.001$ Pa · s, at the assumed height of h. Therefore, the following simple linear approximation was used to obtain the value of the apparent viscosity at the inflection point,

$$\mu_{FSL} = \mu_w + \frac{(\mu_{PL} - \mu_w)(h - \delta_{FSL})}{h}. \quad (2)$$

Figure 3c depicts an example viscosity profile obtained for run 15. Since viscometric flows are laminar, the apparent viscosities obtained following the procedure described in this section are referred to as laminar apparent viscosities.

2.4. Shear Stress Profile

We extend the common definition of the shear stress profile of density flows to density flows containing a plug layer. This stress profile together with the shear rate profile (Figure 3b) are used to obtain a compounded apparent viscosity in section 2.5.

For viscoelastic fluids, the shear stress is composed of a viscous-fluid part and an elastic-solid part (Tanner, 2000). While the viscous-fluid part is dependent on viscosity and velocity gradient, the elastic-solid

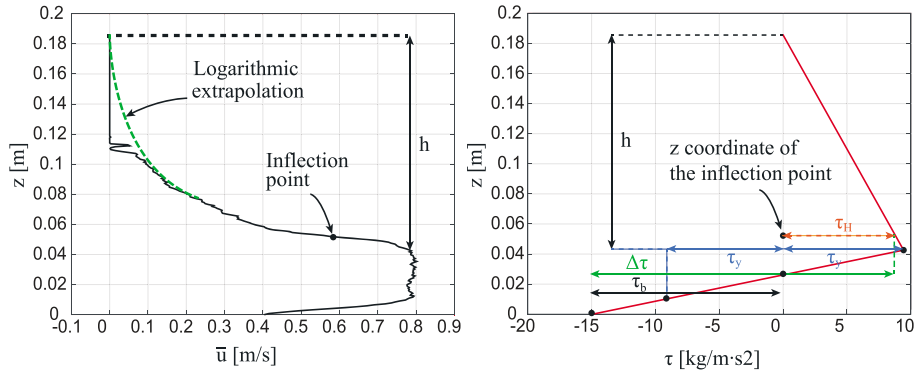

(a) Velocity versus flow height. (b) Stress versus flow height.

Figure 6. Representative example of velocity and stress profiles: (a) Velocity profile and (b) stress profile of run 15. The dashed green line in (a) shows the logarithmic extrapolation of the velocity profile above the location of the Ultrasonic Doppler Velocity profiler. The shear stress at the inflection point, τ_H, the yield stress of the fluid, τ_y, the shear stress at the bed, τ_b, and $\Delta\tau$, are depicted in (b).

part is dependent on the strain and elastic modulus and accounts for the solid deformations that the material undergoes. Within the boundary and free shear layers, the viscous-fluid part dominates. In the plug layer on the other hand, the elastic-solid part prevails. Therefore, in the plug layer the shear stress is predominantly related to the solid deformation of the suspension and not with the viscosity and the velocity gradient.

For a steady flow in equilibrium with only gravity and shear stress forces, the momentum equation can be written as,

$$\left(\rho - \rho_w\right) g \sin\theta = \frac{\mathrm{d}\tau}{\mathrm{d}z}, \tag{3}$$

where ρ and ρ_w are fluid and water densities, and θ is the bed slope. Integrating this equation from the bed to the midpoint of the plug layer, where the stress is assumed to be zero, yields,

$$\left(\rho - \rho_w\right) g \sin\theta \left(\delta_{\mathrm{BL}} + \delta_{\mathrm{PL}}/2\right) = -\tau_b, \tag{4}$$

where τ_b is the stress at the bed.

The top and bottom of the plug layer are the two locations where the shear stress is equal to the yield strength of the plug. Within the boundary layer, the shear stress therefore varies between τ_b at the bed and the yield stress, τ_y, of the plug layer at the height $z = \delta_{\mathrm{BL}}$, with $z = 0$ at the bed. Within the top part of the flow, the shear stress varies between the yield stress, τ_y, of the plug layer at $z = \delta_{\mathrm{BL}} + \delta_{\mathrm{PL}}$, and zero at $z = \delta_{\mathrm{BL}} + \delta_{\mathrm{PL}} + h$.

Using linear approximation, for every run a stress profile can be estimated (Figure 6b). Within this profile τ_H is the approximated stress at the inflection point, τ_y is the fluid yield stress, and $\Delta\tau = |\tau_y| + |\tau_b|$.

2.5. Compounded Apparent Viscosity

Since the stress and the shear rate profiles described in sections 2.4 and 2.2 were derived using velocity data obtained from the UVP probe measurements, they contain the information regarding the regimes of the flows. In this section this information is used to introduce the notion of a compounded apparent.

The viscous-fluid and elastic-solid behaviors of a viscoelastic fluid are encapsulated within the laminar apparent viscosity data obtained from the rheometer. However, within the boundary or the free shear layer, the flow may become unsteady or even turbulent. Therefore, the apparent viscosity maybe considered to be a function of the shear strain, γ, as well as the concentration and the shear rate. For a fluid flowing within the turbulent regime, the flow parameters can be decomposed into a time-averaged quantity denoted by $\bar{}$ and a fluctuating quantity denoted by $'$. Then using Taylor expansion, the apparent viscosity can be written as,

$$\mu(\bar{C} + C', \bar{\gamma} + \gamma', \bar{\dot{\gamma}} + \dot{\gamma}') = \mu(\bar{C}, \bar{\gamma}, \bar{\dot{\gamma}}) + \frac{\partial\mu}{\partial\bar{C}}C' + \frac{\partial\mu}{\partial\bar{\gamma}}\gamma' + \frac{\partial\mu}{\partial\bar{\dot{\gamma}}}\dot{\gamma}' + H.O.T., \tag{5}$$

Inserting equation (5) in (1) and collecting terms yields

$$\tau = \mu(\bar{C} + C', \bar{\gamma} + \gamma', \bar{\dot{\gamma}} + \dot{\gamma}')(\bar{\dot{\gamma}} + \dot{\gamma}') = \overbrace{\mu(\bar{C}, \bar{\gamma}, \bar{\dot{\gamma}})\bar{\dot{\gamma}}}^{\bar{\tau}} + \overbrace{\left(\mu(\bar{C}, \bar{\gamma}, \bar{\dot{\gamma}})\dot{\gamma}' + \frac{\partial \mu}{\partial \bar{C}} C'\bar{\dot{\gamma}} + \frac{\partial \mu}{\partial \bar{\gamma}} \gamma'\bar{\dot{\gamma}} + \dots\right)}^{\tau'}, \tag{6}$$

where $\bar{\tau}$ and τ' are the time-averaged and the fluctuating part of the shear stress, respectively.

Performing a time averaging procedure on the convective terms in the momentum equation results in the extra term $\rho u_i' u_j'$, where $\vec{u} = (u_1, u_2, u_3)$ is the velocity vector and $i, j = 1, 2, 3$. Lumping this expression with the fluctuating part of the shear stress yields

$$\hat{\tau} = \tau + \rho u_i' u_j' = \bar{\tau} + (\tau' + \rho u_i' u_j'). \tag{7}$$

Factoring shear rate out of expression (7) yields

$$\hat{\tau} = \left(\bar{\tau}/\dot{\gamma} + (\tau' + \rho u_i' u_j')/\dot{\gamma}\right)\dot{\gamma} = \overbrace{\left(\mu_l + \mu_t\right)}^{\tilde{\mu}}\dot{\gamma}, \tag{8}$$

where $\tilde{\mu}$ is called the compounded apparent viscosity and is composed of a laminar apparent viscosity, $\mu_l = \bar{\tau}/\dot{\gamma}$, and a turbulent apparent viscosity, $\mu_t = (\tau' + \rho u_i' u_j')/\dot{\gamma}$.

The stress and the shear rate profiles described in sections 2.4 and 2.2 can be used to obtain average compounded apparent viscosities for the boundary layer, $\tilde{\mu}_{BL}$, and the free shear layer, $\tilde{\mu}_{FSL}$, similar to the laminar apparent viscosity data shown in Figure 3c.

The laminar apparent viscosity data obtained from the rheometer tests (section 2.3) correspond to the viscosity of the mixtures within the laminar regime, while the compounded apparent viscosity data computed from the stress and shear rate profiles of Figures 6b and 3b do not make such a restriction regarding the regime of the flow. Therefore, deviation of the former measured viscosity from the computed one is a measure of deviation of a flow from the laminar regime. In other words, this deviation can be seen as a measure of turbulence, albeit a qualitative one due to the approximations followed here. The ratios $\tilde{\mu}_{BL}/\mu_{BL}$ and $\tilde{\mu}_{FSL}/\mu_{FSL}$ will be used to evaluate the regimes of the flows within the boundary and free shear layers, respectively.

Due to the farther distance of the second UVP probe from the inlet compared to the first one, the flow at this location is assumed to be closer to steady equilibrium conditions. Therefore, it is suggested here that the data obtained from the second UVP probe satisfies the assumptions for calculating the compounded apparent viscosity profiles.

2.6. Inner Variable and Existence of Logarithmic Region

Ludwig Prandtl and Theodore von Kármán deduced that a turbulent boundary layer must contain a logarithmic overlap layer (White, 1991). In order to evaluate the existence of a logarithmic overlap region and hence, the state of the flow within the boundary layer, the inner variable

$$z^+ = \frac{z u_* \rho}{\mu_{BL}}, \tag{9}$$

is calculated, where ρ is the density of the mixture within the mixing tank and u_* is the friction velocity approximated by

$$u_* = \sqrt{g\, \tilde{H}\, R\, \phi \sin(\theta)}. \tag{10}$$

In this expression, θ is the bed slope, $\tilde{H} = \frac{WH}{(2H+W)}$ is the hydraulic radius, with $W = 0.1$ m representing the width of the flume (Figure 1), $\phi = \frac{V_s}{V_s+V_w}$ is the sediment volume concentration, with V_s representing the sediment volume, and V_w the volume of water, $R = \frac{\rho_s - \rho_w}{\rho_f}$, with ρ_w representing the water density, ρ_s, the sediment density, and ρ_f the fluid density.

Within the boundary layer, the viscous sublayer and the buffer layer extend from approximately $0 \leq z^+ \leq 30$, and the logarithmic overlap region begins from approximately $30 < z^+$ (White, 1991). Therefore, a turbulent boundary layer containing a logarithmic overlap region is expected to have a maximum inner variable, $z^+_{\delta_{BL}}$, well above 30.

2.7. Reynolds Numbers, Froude Number, and Dimensionless Yield Stress Parameter Definitions

It was found that in order to differentiate various density flows, two Reynolds numbers for the boundary and free shear layers, a Froude number, and a dimensionless yield stress parameter are needed. The Reynolds numbers characterize the laminar or turbulent regime of a flow within the boundary and the free shear layers and are defined as

$$Re_{\mu,\mathrm{FSL}} = \frac{\rho_{\mathrm{FSL}} U(2\delta_{\mathrm{FSL}})}{\mu_{\mathrm{FSL}}}, \tag{11}$$

$$Re_{\mu,BL} = \frac{\rho_{\mathrm{BP}} U\delta_{\mathrm{BL}}}{\mu_{\mathrm{BL}}}, \tag{12}$$

for the free shear layer (subscript FSL) and the boundary layer (subscript BL), respectively. In these expressions, U is the average velocity defined as

$$U = \frac{\int_0^H \bar{u}\, \mathrm{d}z}{H}, \tag{13}$$

and for a specific run was obtained by integrating the interpolated velocity profile of the run (Figure 3a), ρ_{BP} is the density of the mixture within the boundary and plug layers and was assumed to be equal to the density of the mixture within the mixing tank, and ρ_{FSL} is the density of the mixture in the free shear layer.

Within the free shear layer and above the inflection point the density varies between that of the plug layer to that of water at the height $z = \delta_{\mathrm{BL}} + \delta_{\mathrm{PL}} + h$. Therefore, the density at the inflection point was approximated by

$$\rho_{\mathrm{FSL}} = \rho_w + \frac{\left(\rho_{\mathrm{BP}} - \rho_w\right)\left(h - \delta_{\mathrm{FSL}}\right)}{h}. \tag{14}$$

The largest Kelvin-Helmholtz eddies which are created within the free shear layer and which contribute the most to the mixing in this region can be viewed to rotate about the inflection point, as this is the point of maximum vorticity (White, 1991). Therefore, these eddies have a radius that spans from the top of the plug to the inflection point. Their diameter is approximately $2\delta_{\mathrm{FSL}}$.

Following the definitions in (11), the laminar to turbulent transition zone starts at an approximate Reynolds number of 500. This is equivalent to a Reynolds number of 2,000 if the definition of the length scale in (11) is replaced by the hydraulic diameter (Wang & Plate, 1996).

Using the definitions of the average velocity, U, and the flow height, H, the Froude number is defined as

$$Fr = \frac{U}{\sqrt{gH}}. \tag{15}$$

For low concentration density flows the effect of density fluctuations on the inertial term in the momentum equation can be ignored. This is known as the Boussinesq approximation. This approximation falls apart for high concentration density flows. Therefore, a reduced gravity term is not considered here in the definition of the Froude number (Nappo, 2002).

The existence of a plug layer is here characterized by the dimensionless yield stress parameter, $\frac{\tau_y}{\Delta\tau}$, where τ_y and $\Delta\tau$ were defined in section 2.4.

3. Results

3.1. Flow Types

Based on the experimental results four different flow types were observed which are defined by different vertical stacking patterns of flow states. The data sets obtained for runs 18, 20, 22, and 25 exhibit distinct characteristics corresponding to these four different flow types and will be used as examples. In this section the velocity profile, the boundary layer structure, and the free shear layer structure of these four flow types are discussed in detail.

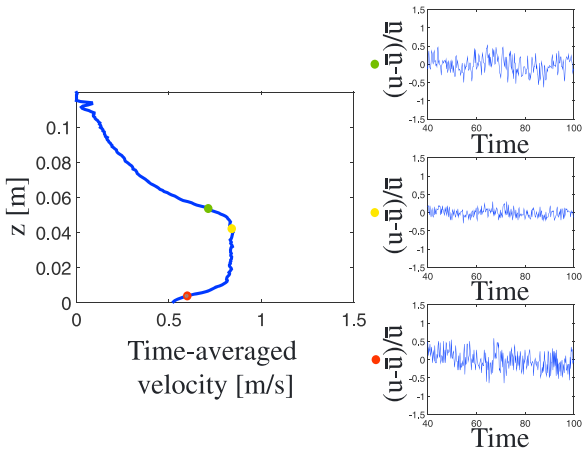

(a) Velocity profile (left) and velocity fluctuations (right) of run 18 at the location of UVP2 probe.

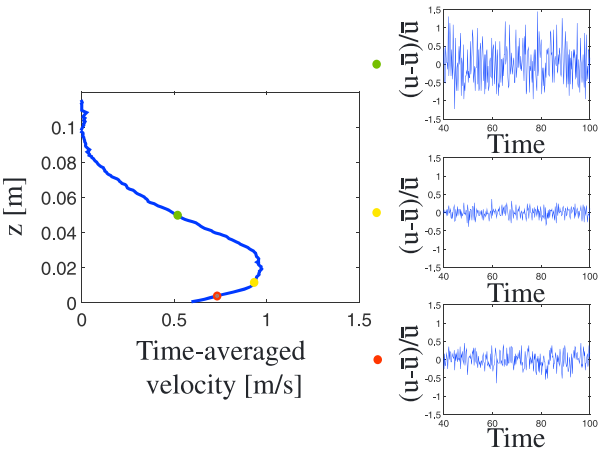

(b) Velocity profile (left) and velocity fluctuations (right) of run 20 at the location of UVP1 probe.

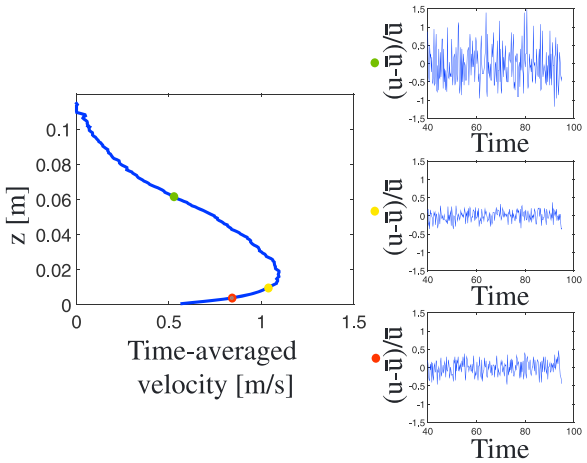

(c) Velocity profile (left) and velocity fluctuations (right) of run 22 at the location of UVP1 probe.

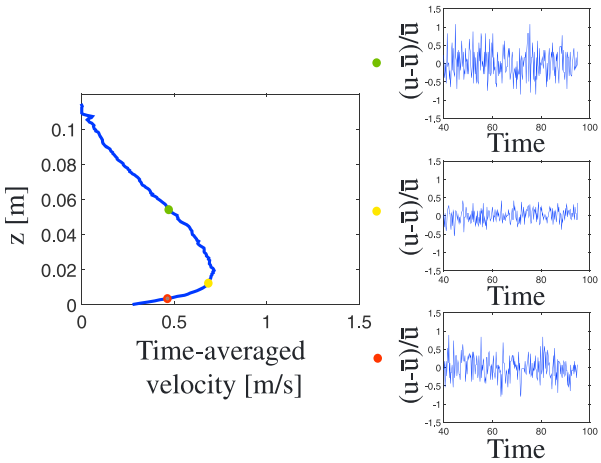

(d) Velocity profile (left) and velocity fluctuations (right) of run 25 at the location of UVP1 probe.

Figure 7. Velocity profiles and fluctuations of runs 18 (a), 20 (b), 22 (c), and 25(d). Normalized velocity fluctuations, $\frac{u-\bar{u}}{\bar{u}}$, are depicted at 3.8 mm from the bed (red), at the point of minimum u'_{rms} (yellow), and at the inflection point (green). UPV = Ultrasonic Doppler Velocity Profiler.

3.1.1. Velocity profile

Figure 7 depicts the velocity profiles of runs 18, 20, 22, and 25. Normalized velocity fluctuations, $\frac{u-\bar{u}}{\bar{u}}$, where u is the recorded velocity and $\bar{u}$ is the time-averaged velocity, are also depicted at 3.8 mm from the bed, at the point of minimum root mean square of velocity fluctuations (u'_{rms}) and at the inflection point in the mixing layer.

Following a length scale analysis, the Kolmogorov length scales, the velocity amplitude spectrum, and the energy spectrum were calculated. Based on this analysis, it was observed that the measurement resolutions were not adequate for performing turbulence intensity calculations. Therefore, the velocity fluctuation data could only provide a qualitative means for the estimation of the level of turbulence.

From Figure 7a it can be observed that for run 18, the magnitude of velocity fluctuations is relatively small within the free shear layer, a large plug layer is visible within the velocity profile of this run, and the magnitude of velocity fluctuations is relatively small within the boundary layer. By contrast the data of run 20 (Figure 7b) shows large velocity fluctuations within the free shear layer. A small plug layer is visible within the velocity profile of this run, and within the boundary layer the magnitude of velocity fluctuations is relatively small. The data for run 22 (Figure 7c) resemble that of run 20, with the exception that no plug layer is visible within

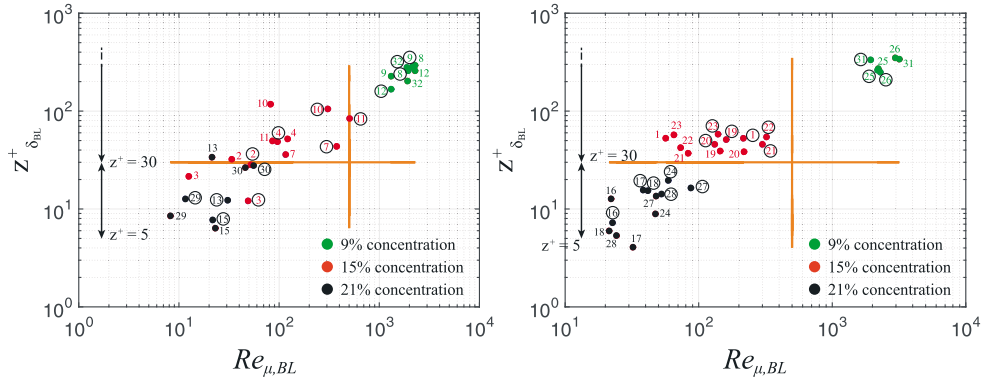

(a) Sand-clay-water runs. (b) Sand-silt-clay-water runs.

Figure 8. Maximum inner variable, $z^+_{\delta_{BL}}$, versus $Re_{\mu,BL}$ for (a) sand-clay-water runs and (b) sand-silt-clay-water runs. The vertical orange lines indicate $Re_{\mu,BL} = 500$. The horizontal orange lines indicate $z^+ = 30$. Dots indicate where different runs are situated in this plot. Run numbers are placed next to their corresponding dots. Encircled run numbers indicate data obtained from the first Ultrasonic Doppler Velocity Profiler probe. Runs with 21% sediment concentration are shown in black, runs with 15% sediment concentration are shown in red, and runs with 9% sediment concentration are shown in green.

the velocity profile of this run. Finally, the data of run 25 (Figure 7d) show relatively large velocity fluctuations within the free shear layer, no plug layer, and relatively large velocity fluctuations within the boundary layer.

3.1.2. Boundary Layer Structure

Figure 8 shows the maximum inner variable versus the boundary layer Reynolds number for different runs. The vertical orange lines in these plots are located at $Re_{\mu,BL} = 500$ and separate the laminar and turbulent regimes. The horizontal orange lines are located at $z^+ = 30$ and indicate termination of the buffer layer and the beginning of the logarithmic overlap region. It can be observed that the boundary layers of the runs with 21% sediment concentration, shown in black, extend from the bed until the end of the buffer layer. The boundary layers of the runs with 15% sediment concentration, shown in red, extend from the bed into the logarithmic region and terminate within this region. The boundary layers of the runs with 9% sediment concentration, shown in green, extend the furthest into the log-law region and have Reynolds numbers higher than 500. Therefore, the data suggest that the boundary layers of these runs are turbulent.

Figure 9 shows the ratio of compounded apparent viscosity, $\tilde{\mu}_{BL}$, obtained as in section 2.5, to the laminar apparent viscosity obtained from rheometer tests, μ_{BL}, versus the boundary layer Reynolds number, $Re_{\mu,BL}$. It can be observed that for higher concentration runs, shown in black and red, the ratio $\tilde{\mu}_{BL}/\mu_{BL}$ is low, indicating low levels of turbulence within the boundary layers of these runs. For the runs with 9% sediment concentration, shown in green, on the other hand, $10 < \tilde{\mu}_{BL}/\mu_{BL}$, indicating higher values of turbulent viscosity and turbulence levels within the boundary layers of these runs.

The velocity fluctuation data, the maximum inner variable plots, and the apparent viscosity results suggest laminar and close to laminar boundary layer conditions for runs 18, 20, and 22, and turbulent boundary layer conditions for run 25.

3.1.3. Free Shear Layer Structure

A characteristic of fully developed turbulent flows is self-similarity (White, 1991). For fully developed turbulent free shear layers, self-similarity entails $\bar{u}_{inf}/\bar{u}_{max} \rightarrow 0.5$, where $\bar{u}_{inf}$ is the time-averaged velocity at the inflection point and $\bar{u}_{max}$ is the maximum time-averaged velocity. Figure 10 shows the plots of $\bar{u}_{inf}/\bar{u}_{max}$ versus $Re_{\mu,FSL}$ for different runs.

It can be observed that the runs with 21% sediment concentration, shown in black, have relatively high values of $\bar{u}_{inf}/\bar{u}_{max}$ and fall within the laminar region. Various runs with 15% sediment concentration, shown in red, have high values of $\bar{u}_{inf}/\bar{u}_{max}$ and fall within the laminar region, while the others have low values of $\bar{u}_{inf}/\bar{u}_{max}$ and fall within the turbulent region. The runs with 9% sediment concentration, shown in green, have $\bar{u}_{inf}/\bar{u}_{max} \lesssim 0.67$ and fall within the turbulent region.

Self-similarity of fully turbulent free shear flows also entails the collapse of all properly scaled free shear layer velocity profiles onto each other. Figure 11a depicts the scaled free shear layers of 11 runs at the location

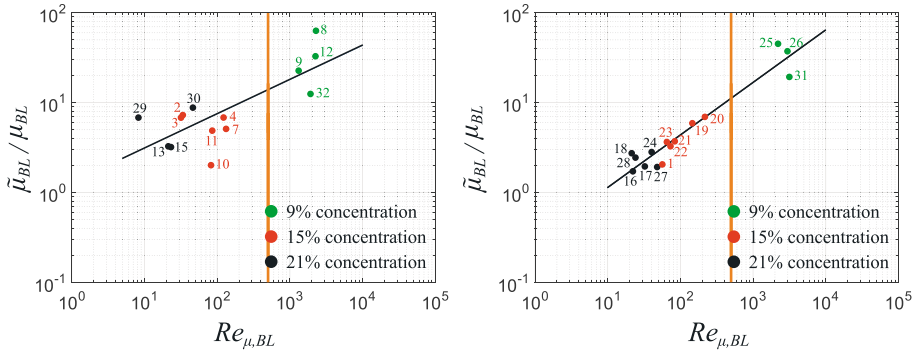

(a) Sand-clay-water runs. (b) Sand-silt-clay-water runs.

Figure 9. $\tilde{\mu}_{BL}/\mu_{BL}$ versus $Re_{\mu,BL}$ for the data gathered from the second Ultrasonic Doppler Velocity Profiler probe for (a) sand-clay-water runs and (b) sand-silt-clay-water runs. The vertical orange line indicates $Re_{\mu,BL} = 500$. Dots indicate where different runs are situated in this plot. Run numbers are placed next to their corresponding dots. Runs with 21% sediment concentration are shown in black, runs with 15% sediment concentration are shown in red, and runs with 9% sediment concentration are shown in green. The black line is a least squares fit to the data.

of the second UVP probe. These 11 runs were chosen out of the total number of runs for the sake of clarity in presentation. In this figure, 0.99 $\bar{u}_{max}$ is the time-averaged velocity above the plug layer (Figure 3a), $\bar{u}(H)$ is the time-averaged velocity at the height H, $\bar{u}$ is the time-averaged velocity with range $[\bar{u}(H), 0.99\ \bar{u}_{max}]$, and z is the distance above the bed and varies between $\delta_{BL} + \delta_{PL}$ and H. It can be seen that the free shear layers of the majority of the runs with 21% sediment concentration fall above those of runs with 15% and 9% sediment concentrations. Figure 11b shows the scaled free shear layers of run 18 at the location of the second UVP probe, and runs 20, 22, and 25 at the location of the first UVP probe. It can be seen that the free shear layer of run 18 is recognizable and falls above those of the other runs. This deviation from the self-similar and hence fully turbulent flow for run 18 is in agreement with the high values of $\bar{u}_{inf}/\bar{u}_{max}$ for this run, and the low velocity fluctuations observed within the free shear layer of this run (Figure 7).

Figure 12 shows the ratio of compounded apparent viscosity within the free shear layer, $\tilde{\mu}_{FSL}$, obtained as in section 2.4, and the laminar apparent viscosity, μ_{FSL}, obtained from rheometer tests, versus the free shear layer Reynolds number, $Re_{\mu,FSL}$.

Similar to the boundary layer results, in Figure 12 it can be observed that for higher concentrations the ratio $\tilde{\mu}_{FSL}/\mu_{FSL}$ decreases toward one. Higher viscosity ratios are reached at higher Reynolds numbers, suggesting higher turbulence levels for more dilute flows within the free shear layer. The increase in viscosity ratio is less pronounced in Figure 12 compared to Figure 9.

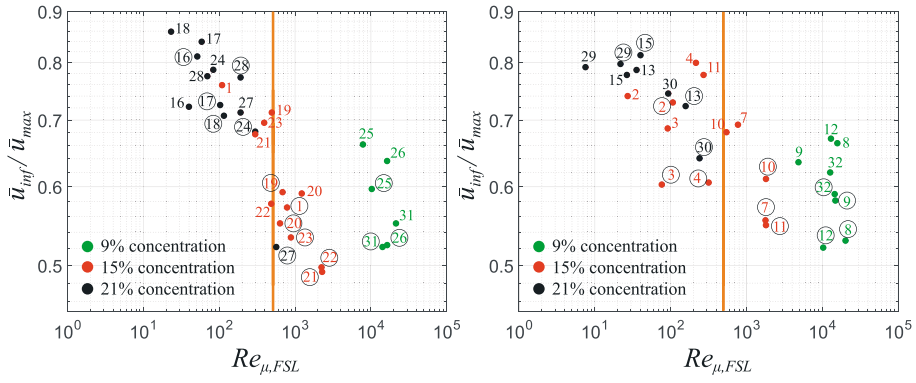

(a) Sand-clay-water runs. (b) Sand-silt-clay-water runs.

Figure 10. Plots of $\bar{u}_{inf}/\bar{u}_{max}$ versus $Re_{\mu,FSL}$ for (a) sand-clay-water runs and (b) sand-silt-clay-water runs. The vertical orange line indicates $Re_{\mu,FSL} = 500$. Dots indicate where different runs are situated in this plot. Run numbers are placed next to their corresponding dots. Encircled run numbers indicate data obtained from the first Ultrasonic Doppler Velocity Profiler probe. Runs with 21% sediment concentration are shown in black, runs with 15% sediment concentration are shown in red, and runs with 9% sediment concentration are shown in green.

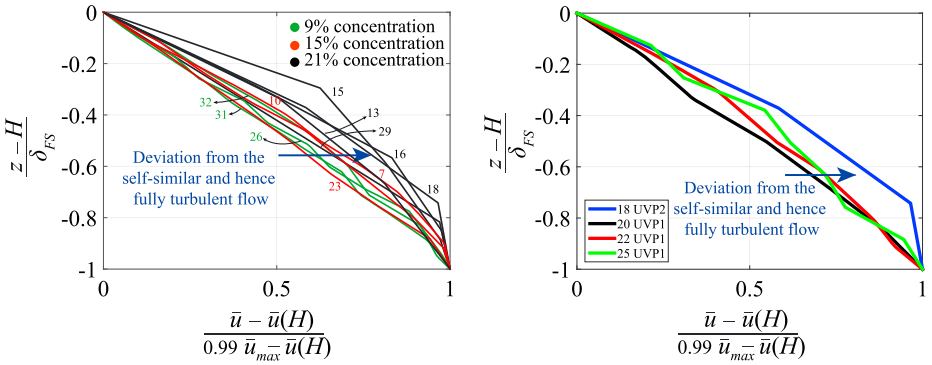

(a) Scaled free shear layers of 11 runs at the location of the second UVP probe.

(b) Scaled free shear layers of run 18, 20, 22, and 25.

Figure 11. Scaled free shear layers for (a) eleven random runs and for (b) the selected runs 18, 20, 22, and 25. In (a), runs with 21% sediment concentration are shown in black, runs with 15% sediment concentration are shown in red, and runs with 9% sediment concentration are shown in green. UPV = Ultrasonic Doppler Velocity Profiler.

Within the free shear layer, the velocity fluctuation data (Figure 7), the self-similarity results (Figures 10 and 11), and the viscosity calculations (Figure 12) suggest laminar conditions for run 18 and turbulent conditions for runs 20, 22, and 25.

3.2. Sediment Deposits

Figure 13 shows the deposits emplaced by the runs in Figure 7. The classification scheme of Talling et al. (2012) is used for each layer, and the classification scheme of Sumner et al. (2009) is used for the complete deposits. The 21% sediment concentration flow of run 18, with a discharge rate of 10 m^3/hr and on a bed slope of 6°, resulted in a very thin basal sand layer that was deposited by the body of the flow at the midsection of the flume (Figure 1). Once the run was close to termination and the discharge rate waned, the tail of the flow resulted in en masse deposition of a thick, uniform, mud-sand mixture throughout the flume, similar to the deposit Type IV of Sumner et al. (2009). A top thin clay drape was deposited from the suspension after the flow stopped. Similar to run 18, the 15% sediment concentration flow of run 20, with a discharge rate of 10 m^3/hr and on a bed slope of 9.5°, resulted in a thin bottom sand layer that was deposited from the body of the flow at the midsection of the flume. Once the run was close to termination and the discharge rate waned, the tail of the flow deposited a mud-sand layer throughout the flume. This layer was thinner compared to the mud-sand layer of run 18. A top thin clay drape was deposited from the suspension after the flow stopped.

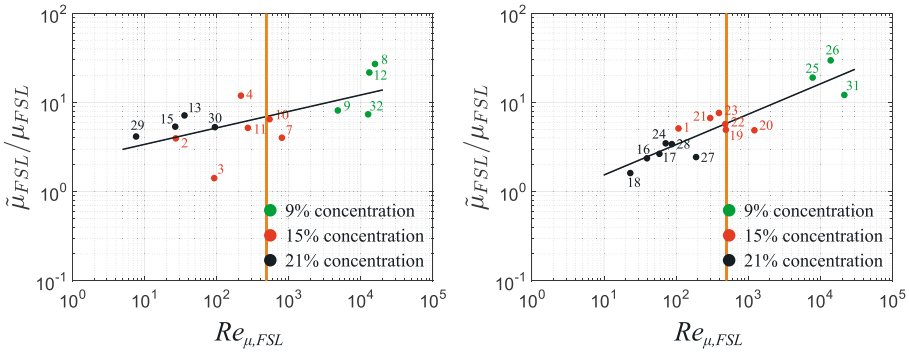

(a) Sand-clay-water runs.

(b) Sand-silt-clay-water runs.

Figure 12. $\tilde{\mu}_{FSL}/\mu_{FSL}$ versus $Re_{\mu,FSL}$ for the data gathered from the second Ultrasonic Doppler Velocity Profiler probe for (a) sand-clay-water runs and (b) sand-silt-clay-water runs. The vertical orange line indicates $Re_{\mu,BL} = 500$. Dots indicate where different runs are situated in this plot. Run numbers are placed next to their corresponding dots. Runs with 21% sediment concentration are shown in black, runs with 15% sediment concentration are shown in red, and runs with 9% sediment concentration are shown in green. The black line is a least squares fit to the data.

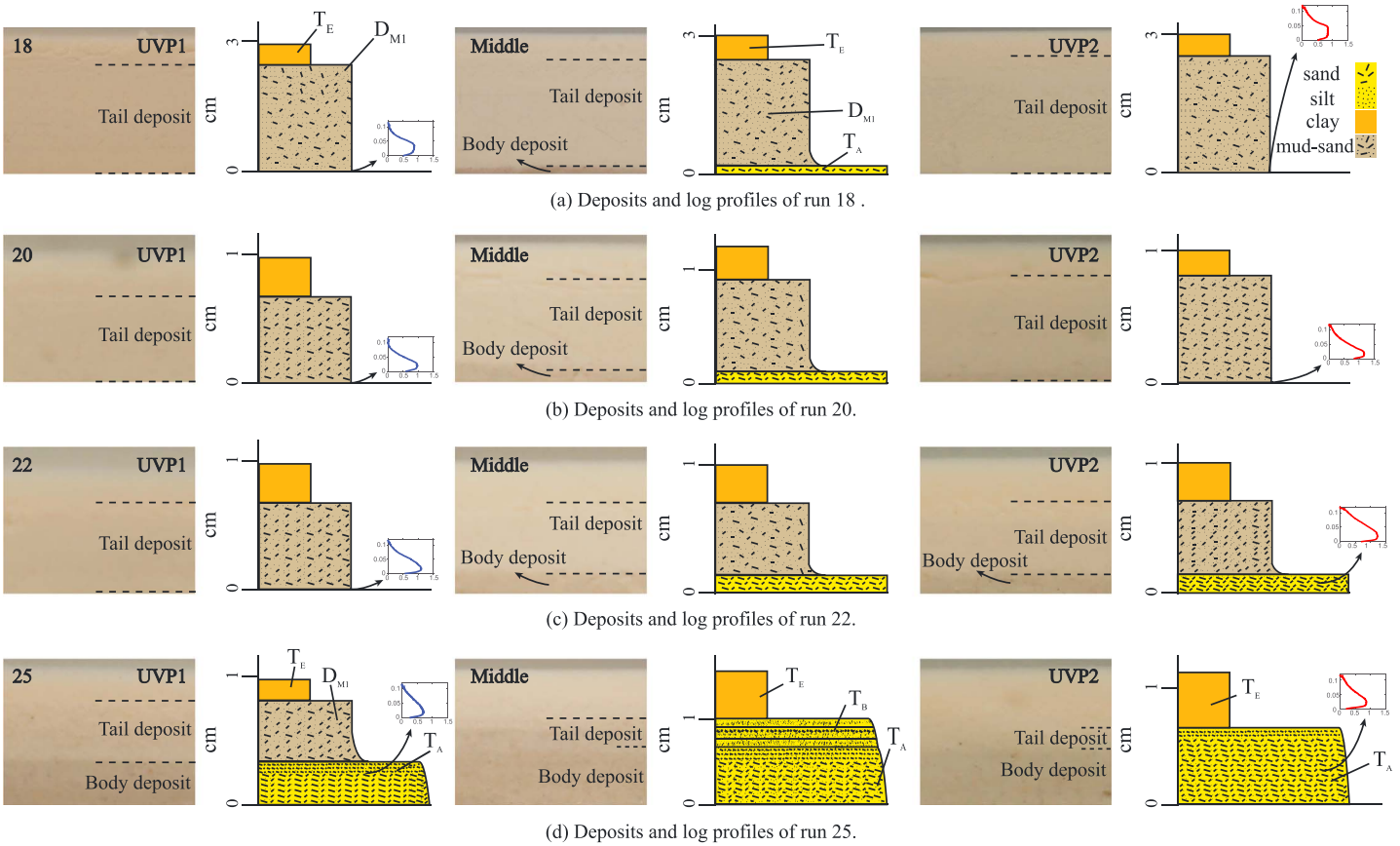

Figure 13. Deposits and log profiles of (a) run 18, (b) run 20, (c) run 22, and (d) run 25, at the location of the first Ultrasonic Doppler Velocity Profiler (UVP) probe (left), at the midsection of the flume (middle), and at the location of the second UVP probe (right). Inset plots depict velocity profiles at the location of the first UVP probe (blue), and the right UVP probe (red). Classification of Talling et al. (2012) is used for the deposit types. T_E: Fine mud, D_{M1}: Mud-sand, T_B: Planar laminae and massive sand, T_A: Massive sand.

Similar to run 18, the deposit from this run resembles the deposit Type IV of Sumner et al. (2009). Moving to a higher discharge rate of 15 m^3/hr and a lower bed slope of 8°, the 15% sediment concentration flow of run 22 resulted in deposition of a bottom sand layer at the midsection of the flume and at the location of the second UVP probe. This sand layer was emplaced by the body of the flow. Once the run was close to termination and the discharge rate waned, the tail of the flow deposited a mud-sand layer throughout the flume. A top thin clay drape was deposited from the suspension after the flow stopped. The deposits from this run at the midsection of the flume and at the location of the second UVP probe resemble the deposit type III of Sumner et al. (2009). The 9% sediment concentration flow of run 25, with a discharge rate of 10 m^3/hr and a bed slope of 6°, resulted in deposition of a bottom sand layer throughout the flume. This sand layer was emplace by the body of the flow. Once the run was close to termination and the discharge rate waned, the tail of the flow deposited a mud-sand layer at the location of the first UVP probe, a planar sand and sand-silt lamination at the midsection of the flume, and a sand layer at the location of the second UVP probe. A top thin clay drape was deposited from the suspension after the flow stopped. The deposit from this run at the midsection of the flume resembles the deposit type I of Sumner et al. (2009). At the location of the second UVP probe, this flow emplaced a deposit similar to the deposit Type II of Sumner et al. (2009).

It can be observed that in moving from run 18 to runs 20 and 22, the mud-sand layer becomes thinner and the basal clean sand layer forms an increasing proportion of the deposit. All in all, in moving from the top toward the bottom in Figure 13, it can be seen that more sand is deposited by the low concentration flows that experienced higher velocity fluctuations within the boundary layer. Furthermore, while the velocity profiles of runs 20 and 22 show different flow structures (Figure 7), their deposits do not differ much.

4. Discussion of Flow Types and the Resulting Deposits

Subaqueous density flows can be classified based on the existence of turbulence within the free shear and/or boundary layer and presence of a plug layer. A dense and cohesive flow whose primary sediment support mechanism is not turbulence and which is laminar within the boundary and free shear layers and contains a plug layer is referred to as a PF (Figure 14a). The inflection point is relatively close to the plug for such a flow (Figure 14a). During the experiments such a flow type resulted in either no deposition or deposition of a thin basal clean sand layer as in the case of run 18 in Figure 13. The thin basal clean sand layer is attributed to the large amount of shearing within the boundary layer, which breaks up the gel structure created by the clay particles and dramatically decreases the yield stress and viscosity of the suspension (Ovarlez et al., 2012). Since the turbulence levels are low within the boundary layer of PFs (i.e., low sand grain support by turbulence), this further facilitates the movement of sand particles through the boundary layer and allows them to settle, resulting in the deposition of a basal clean sand layer during the run. Once the discharge rate waned, within the tail region of the flow the yield stress of the fluid overcame the force of gravity and the flow froze, resulting in en masse deposition of a thick, uniform, mud-sand mixture. A top clay drape was deposited from the suspension after the flow stopped.

Higher slopes, lower sediment concentrations, or higher discharge rates, all amplify Kelvin-Helmholtz instabilities within the free shear layer. As these instabilities become more severe, the top free shear layer becomes turbulent, yet a plug may continue to exist and the boundary layer may remain laminar. This flow is referred to as top transitional PF (TTPF; Figure 14b). If heavier grains are not supported within the turbulent free shear layer, they settle onto the plug layer and mix into the mud-sand mixture. Experiments showed that a TTPF can result in the deposition of a basal clean sand layer during the flow. This layer was covered by a mud-sand deposit from the tail and a mud drape which settled from suspension once the run was terminated.

As the plug erodes away, due to the top and the bottom stresses, within a TTPF, the boundary layer may still remain within the laminar regime because of higher concentrations close to the substrate where it is sheltered from outside fluctuations. When the plug disappears, the velocity profile begins to resemble that of a turbidity current, yet the boundary layer remains laminar. Such a flow is here referred to as a transitional turbidity current (TTC; Figure 14c). Experiments showed that a TTC can result in the deposition of a basal clean sand layer during the flow. This layer was overlain by a uniform mud-sand mixture that was emplaced once the yield stress exceeded the gravitational forces within the tail region of the flow. A mud drape was emplaced on top of the deposits after the runs were terminated.

Finally, more dilution of the flow reduces the ability of the laminar boundary layer to withstand the outside disturbances and transition of the boundary layer is initiated by velocity perturbations induced by fluctuations within the external turbulent free shear layer (Thole & Bogard, 1996). Once the boundary layer transitions from laminar to turbulent, the turbulent free shear layer and boundary layer begin to interact. This interaction is dictated by the size and strength of the eddies within these layers (Hunt et al., 1998; Thole & Bogard, 1996). In this regime the sediment is mainly supported by turbulence and such a flow is referred to as a turbidity current (TC; Figure 14d). Experiments showed that this flow type resulted in deposition of a massive bottom sand layer such as in the deposit of run 25 in Figure 13. This layer was overlain by either a mud-sand mixture or a sand and sand-silt interlamination. In all cases a mud drape was deposited on top of the deposit after the run was terminated.

For turbulent flows in which turbulence levels are high enough to break the gel structure of the clay, the conditions are favorable for the deposition of sand and silt. If turbulence levels are just high enough to support the silt grains, only sand particles will be deposited. On the other hand if the turbulence levels are not high enough to support the silt grains, sand and silt are deposited together. If the flow is on the edge between these two regimes, it may move back and forth between them, that is, moving back and forth between depositing only sand and depositing sand together with silt. Such a flow results in the deposition of sand and sand-silt interlamination as in the deposit of run 25 at the midsection of the flume in Figure 13d. Higher turbulence levels that can support silt grains result in the deposition of clean bottom sand layer as in the deposit of run 25 at the location of the second UVP probe in Figure 13d. On the other hand, lower turbulence levels cannot efficiently separate the sand and silt from the clay and result in the deposition of a mud-sand mixture as in the deposit of run 25 at the location of the first UVP probe in Figure 13d.

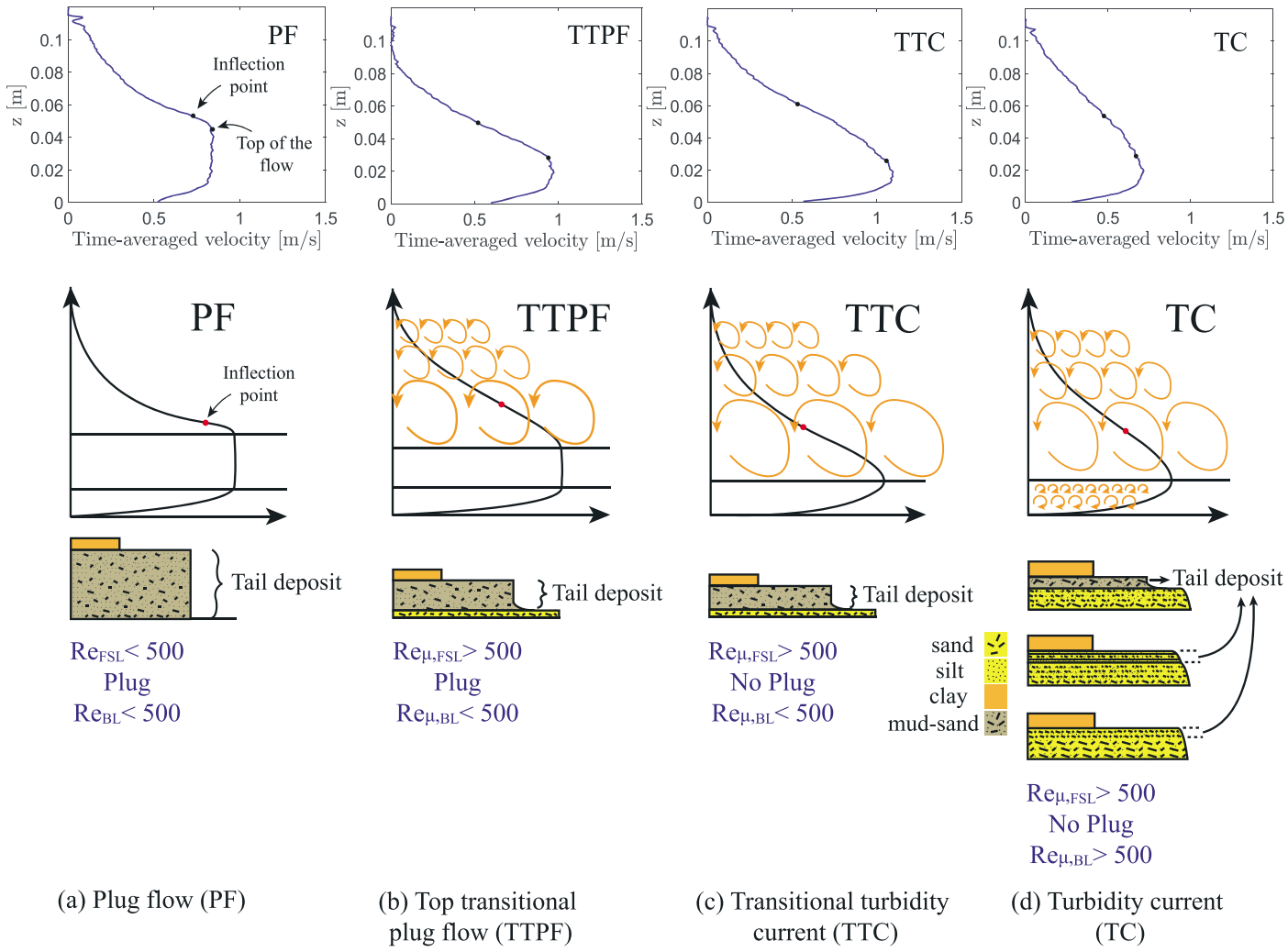

Figure 14. Velocity profiles (top), schematics of the flow structures (middle), and log profiles of the deposits (bottom) of, (a) a plug flow (PF), (b) a top transitional PF (TTPF), (c) a transitional turbidity current (TTC), and, (d) a turbidity current (TC). The orange arrows indicate turbulent regions with Reynolds numbers higher than 500. Three deposit types were observed for TCs, as was explained in Figure 13 for run 25.

The deposits investigated in this study show that both the effect of the flow type and rheology as well as the time evolution of the passage of flow are important in the formation of the structures within a deposit. The deposit emplaced by a flow in steady state at a certain location is solely dependent on the structure of the flow at that location. For clay-rich flows, however, the deposits are mainly the result of a time-dependent decrease in the flow height and dominance of the yield strength of the fluid over the force of gravity. For dilute clay-laden flows, time dependence may be in the form of fluctuations in the turbulence levels which manifests itself in the form of laminations within the deposit. All in all, the structure of the deposit at a location is a result of the flow structures at that location as well as the time-dependent variations in the flow height and turbulence levels.

Table 2 presents different flow types resulting from permutation of flow states within the boundary and free shear layers and the presence or absence of a plug layer.

From the table it becomes apparent that the flows observed in this study correspond to a subset of a wider range of possible flow structures. However, the cases *X*1 to *X*3 can be argued to have low probabilities of occurrence, as will be explained in the following paragraphs. The table also hypothesizes the existence of a top and base transitional PF (TBTPF) with a turbulent free shear layer, a plug layer, and a turbulent boundary layer. Although such a flow was not observed in this study, its existence is hypothesized here. The flow types

Table 2
Flow Types Resulting From Permutation of Flow States Within the Boundary and Free Shear Layers and the Presence or Absence of a Plug Layer

Flow type	FSL	BL	Plug
Plug flow	Laminar	Laminar	Yes
Top transitional plug flow	Turbulent	Laminar	Yes
X1	Laminar	Turbulent	Yes
Top and base transitional plug flow	Turbulent	Turbulent	Yes
X2	Laminar	Laminar	No
Transitional turbidity current	Turbulent	Laminar	No
X3	Laminar	Turbulent	No
Turbidity current	Turbulent	Turbulent	No

Note. The abbreviations stand for free shear layer (FSL) and boundary layer (BL). Flow types denoted by X1, X2, and X3 have arguably low probabilities of occurrence.

in the classification of Baas et al. (2009) for subaerial flows extensively classify the evolutionary stages of a turbulent boundary layer in the vicinity of a plug layer and therefore cover the plug and boundary layer regions of a TBTPF. However, more work is needed to demonstrate the occurrence and characteristics of TBTPFs.

The cases *X*1 and *X*3 in Table 2 are predicted to have a laminar free shear layer and a turbulent boundary layer. The existence of an inflection point within the velocity profile of the free shear layer results in the existence of inviscid instability and possibly a lower critical Reynolds number (White, 1991). Although, this effect may to some extent be counteracted by the stratification and influence of the buoyant force on suppressing the growth of disturbances (Nappo, 2002), the inviscid instability theory suggests possibly earlier transition of the free shear layer to turbulence than the boundary layer. Therefore, a flow with a laminar free shear layer and a turbulent boundary layer, cases *X*1 and *X*3 in Table 2, seems to have a low probability occurring.

The case *X*2 in Table 2 is predicted to have a laminar free shear layer, no plug layer, and a laminar boundary layer. From equation (3), for a subaerial clay-laden flow in equilibrium conditions with only gravitational and shear stress forces one has

$$\left(\rho - \rho_w\right) g \sin\theta \left(H - \delta_{\mathrm{BL}}\right) = \tau_y, \tag{16}$$

where H is the flow height. From equation (16), it can be deduced that for a yield stress fluid, that is, $\tau_y \neq 0$, with no shearing at the top, the plug layer cannot disappear, that is, $\left(H - \delta_{\mathrm{BL}}\right) \neq 0$. For a subaqueous clay-laden flow the plug may be sheared away by the stresses at the top. However, then the density must be high enough for the gravitational force of the sheared laminar top layer to overcome the fluid yield stress and hence induce a flow, and low enough to avoid a plug layer to be created. Such a flow, case *X*2 in Table 2, seems to have a low probability of occurrence.

5. Flow Regime

In order to connect the regimes of each flow type introduced here with those of analogue large-scale flows in nature, appropriate scaling parameters are necessary. Scaling of the boundary and free shear layers can be achieved using the usual Reynolds and Froude numbers. Furthermore, the evaluation of the existence of a plug region is accomplished here with the dimensionless parameter $\tau_y/\Delta\tau$ (Figure 6). In this way, a flow type can be associated with a natural large-scale density flow, or vice versa, using a Froude number, two Reynolds numbers, and a nondimensional yield stress parameter, $\tau_y/\Delta\tau$.

5.1. Boundary Layer Scaling

Figure 15 depicts the boundary layer Reynolds number versus the Froude number for all the runs. The orange line corresponds to the beginning of the turbulent region with a Reynolds number of 500.

The four observed flow types, PF, TTPF, TTC, and TC, are marked by yellow, orange, brown, and green, respectively. Moving from the left to the right in Figure 15, it can be seen that PFs dominate the regions with low boundary layer Reynolds and Froude number. On average, TTPFs and TTCs have higher boundary layer

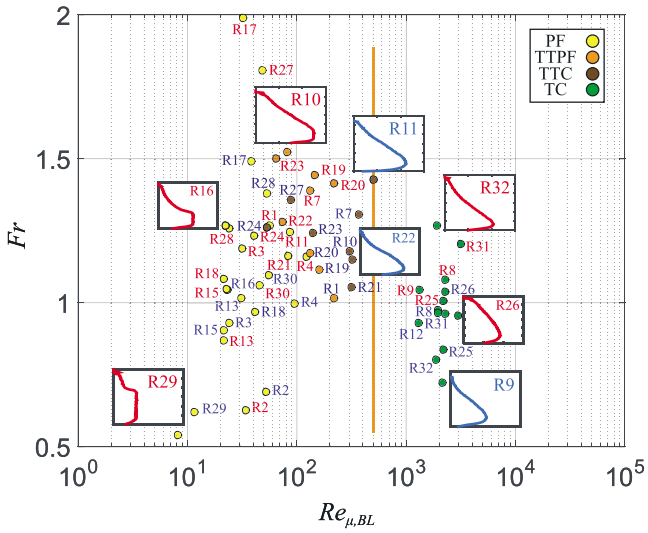

Figure 15. Froude number versus boundary layer Reynolds number for all the runs. Inset plots are the velocity profiles of the runs obtained from the first (blue) and the second (red) Ultrasonic Doppler Velocity Profiler probes. Circles represent where each run is situated within the plot. The run numbers are shown next to each circle and represent the data from the first (blue) or the second (red) UVP probes. The yellow, orange, brown, and green colors represent the flow type corresponding to each run. The orange line separates the laminar from the turbulent flow regime. PF = plug flow; TTPF = top transitional PF; TTC = transitional turbidity current; TC = turbidity current.

Reynolds and Froude numbers compared to PFs. The separation of TTPFs from TTCs is not very clear. TCs dominate the high boundary layer Reynolds number regions of the figure and on average seem to have lower Froude numbers compared to TTPFs and TTCs.

The inset plots in Figure 15 are the velocity profiles of selected runs. It can be seen that by moving from PFs toward TTPFs, the plug layer diminishes in size and finally disappears for TTCs and TCs.

5.2. Free Shear Layer Scaling

Figure 16 depicts the free shear layer Reynolds number versus the Froude number for all the runs.

The flow types in this figure follow a trend similar to that of Figure 15. PFs dominate the regions with low free shear layer Reynolds and Froude number. On average, TTPFs and TTCs have higher free shear layer Reynolds and Froude numbers compared to PFs. The separation of TTPFs from TTCs seems to be better than in Figure 15. TCs dominate the high free shear layer Reynolds number regions of the figure.

The inset plots in Figure 16 are the velocity profiles of selected runs and represent each flow type. The log profiles of the deposits that were emplaced by the majority of the runs, containing the different flow types, are also depicted. Moving from low to high Reynolds numbers, it can be seen that the thick mud-sand deposit that is present for clay-rich flows diminishes in thickness and more sand is deposited from the body of the flow. TCs result in the deposition of most sand. However, at high Reynolds numbers very little deposit is emplaced by the TCs and most of the sediment is bypassed into the basin.

5.3. Plug Layer Scaling

In order to classify a flow as a TTC or as a TTPF, it is necessary to relate the existence of a plug layer to the physical properties of a density flow. Figure 17 depicts the nondimensional yield stress parameter, $\frac{\tau_y}{\Delta\tau}$, as a function of the boundary layer Reynolds number for all the runs. The data in this figure suggest that below the approximate value of $\frac{\tau_y}{\Delta\tau} = 0.25$ the plug layer disappears. This threshold is depicted with a dashed horizontal line to convey that this boundary may not be a horizontal or a linear boundary.

5.4. Discussion of Scaling Parameters

In this study density flows are treated as flows of non-Newtonian fluids. Writing the Navier-Stokes equations for such flows and scaling the equations results in Reynolds and Froude numbers as scaling parameters. The complexities which arise due to various stresses that accompany momentum transport within the mixture (Iverson, 1997) are buried in the apparent viscosity term here obtained from rheometry experiments. The complication which arises here is the problem of connecting the scaling parameters that characterize very low

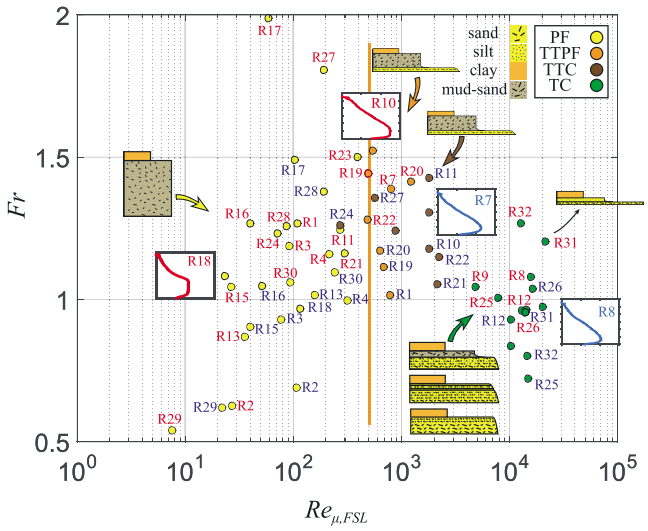

Figure 16. Froude number versus free shear layer Reynolds number for all the runs. Inset plots are the velocity profiles of the runs obtained from the first (blue) and the second (red) Ultrasonic Doppler Velocity Profiler (UVP) probes. Circles represent where each run is situated within the plot. The run numbers are shown next to each circle and represent the data from the first (blue) or the second (red) UVP probes. The yellow, orange, brown, and green colors represent the flow type corresponding to each run. The orange line separates the laminar from the turbulent flow regime. The log profiles of the deposits that were emplaced by the majority of the runs, corresponding to the different flow types, are also depicted. Three deposit types were observed for TCs, as was explained in Figure 13 for run 25. PF = plug flow; TTPF = top transitional PF; TTC = transitional turbidity current; TC = turbidity current.

concentration turbulent flows to the scaling parameters that characterize clay-rich laminar flows. An attempt to overcome this complication, which has been followed here, is to separate the flows into regions with different flow regimes, that is, a free shear layer, a plug layer, and a boundary layer. The free shear and boundary layers in general have different Reynolds numbers, and consequently, one may be laminar while the other is turbulent.

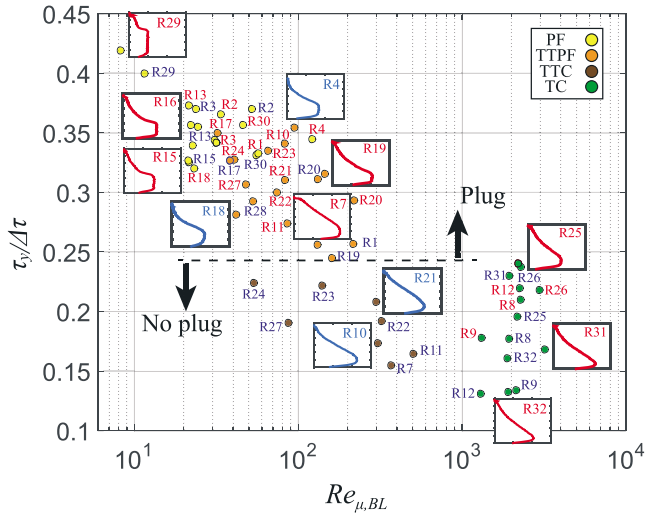

Figure 17. Nondimensional yield stress parameter as a function of boundary layer Reynolds number for all the runs. Inset plots are velocity profiles of the runs obtained from the first (blue) and the second (red) UVP probes. Circles represent where each run is situated within the plot. The run numbers are shown next to each circle and represent the data from the first (blue) or the second (red) UVP probes. The yellow, orange, brown, and green colors represent the flow type corresponding to each run. The horizontal line separates the regions where a plug exists from where it does not. The line is dashed to convey that this boundary may be a sloping or a curved line. PF = plug flow; TTPF = top transitional PF; TTC = transitional turbidity current; TC = turbidity current.

Figures 15 and 16 show that PFs dominate the low Reynolds and Froude number regions. On average, TTPFs and TTCs have higher Reynolds and Froude numbers compared to PFs. TCs dominate the high Reynolds number regions of the figures and on average seem to have lower Froude numbers compared to TTPFs and TTCs.

For TCs, the Reynolds Number crucially controls the deposits. Flows with higher Reynolds numbers support more sand, while flows with lower Reynolds numbers do not efficiently separate the sand from the clay, and hence, result in the deposition of mud-sand mixtures. Figure 16 suggests that there exists a TC with certain Reynolds and Froude numbers which can result in the maximum clean sand deposition.

The fact that at approximately $\frac{\tau_y}{\Delta\tau} < 0.25$ the plug layer disappears is reminiscent of the Richardson number criterion of stability which states that dynamic instability occurs for $0 \leq Ri \leq 1/4$, while for $1/4 < Ri$ the flow is stable (Nappo, 2002). This point, however, requires further investigation.

6. Conclusions

Based on the state of the free shear and boundary layers and existence of a plug, a clay-rich density flow may fall within one of four distinct flow types: (1) a clay-rich PF, (2) a TTPF, (3) a TTC, and (4) a turbulent turbidity current (TC). These flow types were observed in this study, and we have demonstrated that they can be distinguished in measurements performed on experimental density flows.

It was observed that clay-rich PFs resulted in either no deposition or deposition of a thin bottom sand layer. TTPFs and TTCs were mostly characterized by a thin bottom sand layer. The bottom sand layers in PFs, TTPFs, and TTCs were overlain by a mud-sand mixture that was emplaced by the tail of the flow. TCs resulted in the deposition of a thick massive bottom sand layer which was overlain by either a mud-sand mixture or a sand and silt planar lamination from the tail of the flow. In all cases a mud drape was deposited on top of the deposits after the runs were terminated.

The free shear and boundary layers in general have different Reynolds numbers, and consequently, one may be laminar while the other is turbulent. PFs on average have lower Reynolds and Froude numbers compared to TTPFs and TTCs. TCs have the highest Reynolds numbers. However, on average they seem to have lower Froude numbers compared to TTPFs and TTCs.

It was observed that in moving from low to high Reynolds numbers, the thick mud-sand deposit that is emplaced by the tail of the flow diminishes in thickness and more sand is deposited from the body. At high Reynolds numbers turbulent energy can be high enough to support the heavier grains. As a result, very little deposit may be emplaced by the flow. Flows with low Reynolds numbers, on the other hand, do not have enough turbulent energy to efficiently separate the sand from the clay, and hence, result in very little sand deposition. Therefore, the Reynolds versus Froude number plots suggest the existence of a flow within the turbulent regime that may produce clean sand deposits.

The Fr, Re_{BL}, Re_{FSL}, and $\tau_y/\Delta\tau$ parameter space presented here can be used to separate flow types and to connect the small-scale flume experiments to large-scale natural flows. The establishment of regime maps of our classification will allow numerical modelers to determine whether their flows are in a conventional TC regime or whether they need to account for any of the more complex structures arising from the clay in the flows. The linkage between flow structures and depositional characteristics will enable better flow process interpretations from hybrid bed sequences studied by outcrop sedimentologists. Application of the results of this study to large-scale natural flows and their deposits is the scope of future research.

Acknowledgments
We would like to thank The Netherlands Research Center For Integrated Solid Earth Science (ISES) for funding this project. We are grateful to H. K. J. Heller, A. Middeldorp, and A. D. Schuit for their technical assistance in obtaining the rheometry data. We thank J. de Leeuw and J. Trabucho-Alexandre at Utrecht University for their assistance in using the flume and their helpful discussions and inputs. We would also like to show our gratitude to the reviewers who, through their invaluable comments, helped us tremendously in streamlining our ideas to the readers. The processed data set is available at https://doi.org/10.17882/54834.

References

Altinakar, M., Graf, W., & Hopfinger, E. (1996). Flow structure in turbidity currents. *Journal of Hydraulic Research*, *34*(5), 713–718. https://doi.org/10.1080/00221689609498467

Arai, K., Naruse, H., Miura, R., Kawamura, K., Hino, R., Ito, Y., et al. (2013). Tsunami-generated turbidity current of the 2011 Tohoku-Oki earthquake. *Geology*, *41*(11), 1195–1198. https://doi.org/10.1130/G34777.1

Baas, J., Best, J., Peakall, J., & Wang, M. (2009). A phase diagram for turbulent, transitional and laminar clay suspension flows. *Journal of Sedimentary Research*, *79*, 162–183. https://doi.org/10.2110/jsr.2009.025

Baas, J. H., Best, J. L., & Peakall, J. (2011). Depositional processes, bedform development and hybrid bed formation in rapidly decelerated cohesive (mud-sand) sediment flows. *Sedimentology*, *58*, 1953–1987. https://doi.org/10.1111/j.1365-3091.2011.01247.x

Coussot, P. (1997). *Mudflow rheology and dynamics*. Rotterdam: A. A. Balkema.

Felix, M., Leszczyński, S., Ślaczka, A., Uchman, A., Amy, L., & Peakall, J. (2009). Field expressions of the transformation of debris flows into turbidity currents, with examples from the Polish Carpathians and the French Maritime Alps. *Marine and Petroleum Geology*, *26*(10), 2011–2020. https://doi.org/10.1016/j.marpetgeo.2009.02.014

Haughton, P., Davis, C., McCaffrey, W., & Barker, S. (2009). Hybrid sediment gravity flow deposits—Classification, origin and significance. *Marine and Petroleum Geology*, *26*(10), 1900–1918. https://doi.org/10.1016/j.marpetgeo.2009. 02.012

Hunt, J. C. R., Durbin, P. A., & Wu, X. (1998). *Interactions between freestream turbulence and boundary layers*. Retrieved from https://pdfs.semanticscholar.org/45b6/f1c68b10c28020f8544d67ee2146331881d2.pdf

Islam, M. A., & Imran, J. (2010). Vertical structure of continuous release saline and turbidity currents. *Journal of Geophysical Research*, *115*, C08025. https://doi.org/10.1029/2009JC005365

Iverson, R. M. (1997). The physics of debris flows. *Reviews of Geophysics*, *35*, 245–296.

Kane, I. A., & Pontén, A. S. M. (2012). Submarine transitional flow deposits in the Paleogene Gulf of Mexico. *Geology*, *40*, 1119–1122. https://doi.org/10.1130/G33410.1

Kane, I. A., Pontén, A. S. M., Vangdal, B., Joris, T., Hodgson, D. M., & Spychala, Y. T. (2016). The stratigraphic record and processes of turbidity current transformation across deep-marine lobes. *Sedimentology*, *64*, 1236–1273. https://doi.org/10.1111/sed.12346

Kneller, C., Bennett, S. J., & Mccaffrey, W. D. (1999). Velocity structure, turbulence and fluid stresses in experimental gravity currents. *Journal of Geophysical Research*, *104*(1998), 5381–5391.

Manica, R. (2012). Sediment gravity flows: Study based on experimental simulations. In H. Schulz (Ed.), *Hydrodynamics* (pp. 263–286). https://doi.org/10.5772/28794

Meiburg, E., & Kneller, B. (2010). Turbidity currents and their deposits. *Annual Review of Fluid Mechanics*, *42*, 135–156. https://doi.org/10.1146/annurev-fluid-121108-145618

Mohrig, D., Whipple, K. X., Hondzo, M., Ellis, C., & Parker, G. (1998). Hydroplaning of subaqueous debris flows. *Geology*, *110*(3), 387–394.

Mulder, T., & Cochonat, P. (1996). Classification of offshore mass movements. *Journal of Sedimentary Research*, *66*(1), 43–57.

Nappo, C. J. (2002). *An introduction to atmospheric gravity waves*. San Diego: Academic Press.

Ovarlez, G., Bertrand, F., Coussot, P., & Chateau, X. (2012). Shear-induced sedimentation in yield stress fluids. *Journal of Non-Newtonian Fluid Mechanics*, *177–178*, 19–28. https://doi.org/10.1016/j.jnnfm.2012.03.013

Pratson, L. F., Imran, J., Parker, G., Syvitski, J. P. M., & Hutton, E. (2000). Debris flows versus turbidity currents: A modeling comparison of their dynamics and deposits. *AAPG Bulletin*, *84*(2000), 57–71. https://doi.org/10.1306/A9672B86-1738-11D7-8645000102C1865D

Schwarz, H. U. (1982). *Subaqueous slope failures: Experiments and modern occurrences*. Stuttgart: Schweizerbart Science Publishers.

Stow, D. A. V., & Mayall, M. (2000). Deep-water sedimentary systems: New models for the 21st century. *Marine and Petroleum Geology*, *17*(2), 125–135. https://doi.org/10.1016/S0264-8172(99)00064-1

Sumner, E. J., Talling, P. J., & Amy, L. A. (2009). Deposits of flows transitional between turbidity current and debris flow. *Geology*, *37*(11), 991–994. https://doi.org/10.1130/G30059A.1

Talling, P. J., Masson, D. G., Sumner, E. J., & Malgesini, G. (2012). Subaqueous sediment density flows: Depositional processes and deposit types. *Sedimentology*, *59*, 1937–2003. https://doi.org/10.1111/j.1365-3091. 2012.01353.x

Talling, P. J., Wynn, R. B., Masson, D. G., Frenz, M., Cronin, B. T., Schiebel, R., et al. (2007). Onset of submarine debris flow deposition far from original giant landslide. *Nature*, *450*(7169), 541–544. https://doi.org/10.1038/nature06313

Tanner, R. I. (2000). *Engineering rheology*. Oxford Engineering Science Series: OUP Oxford.

Thole, K. A., & Bogard, D. G. (1996). High freestream turbulence effects on turbulent boundary layers. *Journal of Fluids Engineering*, *118*(2), 276–284.

Wang, P. Z., & Plate, P. D. E. C. H. J. (1996). A preliminary study on the turbulence structure of flows of non-Newtonian fluid. *Journal of Hydraulic Research*, *34*(3), 345–361. https://doi.org/10.1080/00221689609498484

White, F. M. (1991). *Viscous fluid flow*. McGraw-Hill International Editions: McGraw-Hill.